11

Advanced Materials for Soft Robotics

Li Wen,[1,*] *Daniel Vogt,*[2] *Zhenyun Shi,*[3] *Qi Shen*[4] and *Ziyu Ren*[5]

ABSTRACT

Soft robotics, a novel member of the robotic family, may apply a rich variety of flexible, advanced materials to generate movements and sense the motion. This new robotic technology delivers a variety of vital applications that can interact safely with human beings and function effectively in complex natural environments, including assistive medical and rehabilitation devices, search and rescue, underwater exploration, space manipulation, industrial operation, etc. Our understanding of the soft robotics is still in its

[1] Department of Mechanical Engineering and Automation, International Research Institute for Multidisciplinary Science, Beihang University, Beijing, 100191, China.
[2] Wyss Institute for Biologically Inspired Engineering, Harvard University, Cambridge, MA 02138, USA.
Email: dvogt@seas.harvard.edu
[3] Department of Mechanical Engineering and Automation, Beihang University, Beijing, 100191, China.
Email: shichong1983623@hotmail.com
[4] Department of Mechanical Engineering, University of Nevada, Las Vegas, NV 89154-4027, USA.
Email: qi.shen@unlv.edu
[5] School of Mechanical Engineering and Automation, Beihang University, Beijing, 100191, China.
Email: renziyu2013@gmail.com
* Corresponding author: liwen@buaa.edu.cn

infancy, the development of advanced materials that can be applied to soft robotics remain a key challenge. This chapter "Advanced materials for soft robotics" aims to meet the urgent requirements for research on advanced materials such as shape memory alloy, stretchable elastomeric sensor and Ionic Polymer-Metal composite that have very recently been used for soft robotics. Theoretical modeling, design, fabrication and experimental characterization included in this chapter could contribute to training of graduate students, robotic engineers and research scientists for understanding fundamental principles of advanced materials and how to apply advanced materials to robotics using a multidisciplinary science based approach.

1. New Trends in Robotics: Soft Robotics

Conventional robots have the capability of operating heavy weights and moving rapidly, but are poor at dealing with human beings, with tissue, with soft objects and objects of complex three-dimensional shapes. The state-of-art of soft robotics inspired a new wave of robotics, and is an innovative research field dedicated to the science and engineering of new advanced materials in machines. In order to interact with various natural environments, multidisciplinary in scope, *Soft Robotics* combines advances in biomedical engineering, biomechanics, material science, soft matter physics and artificial intelligence to provide comprehensive coverage of new approaches to construct devices that can undergo dramatic changes in shape, size, kinematics as well as other functions. In this chapter, we first provide a brief general overview of the advanced materials that can be applied to the soft robotics, then we introduce three representative advanced materials as new forms of actuators and sensors as well as some potential applications. Finally we end up with a discussion of the future perspectives of the soft robotics. This new technology delivers vital applications for a variety of purposes, including search and rescue field robotics, aeronautics space manipulation, industrial operation, assistive medical and rehabilitation devices, etc.

With growing interests in flexible origami of animals such as fish, octopus, jellyfish and caterpillar, etc., smart actuators and sensors have been developed to possess the several principal characteristics: high energy density, light weight and ease to fabricate. Definition of advanced materials, such as shape memory alloy, stretchable elastomeric material and Ionic Polymer-Metal composite and other new forms of both actuation and sensing would be critical to the development of Soft Robotics. In this chapter, we have introduced three representative flexible and advanced materials as new forms of actuators and sensors: Shape memory alloy, eGaIn elastomeric sensor and Ionic Polymer Metal Composites.

The shape memory alloy actuator is a representative actuating material due to its high mass-specific force, it can be widely used as the actuation element of a soft robot. Therefore it is chosen to be covered in this chapter. Further, sensors are essential for robots to interact with the world. Specific to soft robotics, which manipulating deformable and delicate conformal objects, the sensors embedded in soft robotics should be compliant in order to keep the entire system flexible and stretchable. Soft sensors containing micro-channels filled with eutectic Gallium Indium fluid (eGaIn) offer outstanding performance in terms of compliancy and electrical properties. This new type of soft sensor that can provide information of strain, pressure, curvature and shear, which is superb to previous flexible sensors, will be introduced in this chapter as well. Finally, we introduced Ionic Polymer Metal Composites (IPMC), which are made of an ionic polymer membrane with plated gold as electrodes chemically on both sides, which has the advantages of small activation voltage, low noise, and flexibility. These features promise IPMC potential applications on the miniature soft robots as function of both sensors & actuators.

2. Shape Memory Alloys for Soft Robotics

Shape memory alloys (SMAs) can generate force and actuation during the shape recovery process under heating, which makes the shape memory effect an important and innovative actuation principle in the micro robot system. The output force and driving pattern of the SMA actuator is based on the dimensions and shape of the actuator unit, which has shown excellent design flexibility on the joints of wider style robot systems. With growing interests in flexible structures such as fish fins, octopus tentacles, and creeping robots, SMA actuators have been developed to possess the following characteristics: high energy density, specific power and ease of fabrication. As a typical advanced material, a SMA unit can be applied both as an actuator and a sensor at the same time, making the unit a good substitute for muscles and nerves in soft robotics. In particular, the ductile deformation of SMA wires or slices can achieve flexible driving based on structural design. Its high power density supplies flexible design solutions, which can be implanted into tiny structures and maintain the adequate output. Various fabrication methodologies have been studied for combining the SMA unit with soft materials.

Shape memory alloys retain the memory of their original shape and can return to the pre-deformed shape after being heated to a critical temperature. A crystal phase transition appears during the temperature change and causes the materials to change between the high temperature phase (austenite) and the low temperature phase (martensite) and three different crystal structures (twinned martensite, detwinned martensite, and austenite) are

included in the phase change (Fremond 1996). Below the martensite starting temperature, the SMA structure has low stiffness and inelastic straining. Above the austenite starting temperature, the shape memory effect (SME) appears by eliminating the detwinning strain; the maximum recoverable strain can be around 5%. Besides Young's modulus, these two phases also demonstrate obvious differences in thermal conductivity and resistivity.

Many different types of SMA materials were used for industry applications, including nickel-titanium-based and other iron-based and copper-based SMAs such as Fe-Mn-Si, Cu-Zn-Al, and Cu-Al-Ni. Other SMAs are more commercially available and are less expensive than the NiTi-based, but NiTi-based SMAs are most widely applied for better stability, feasibility, superior thermo mechanical performance, and biocompatibility. Most of the actuators and sensors discussed below are applications of NiTi, although NiTiCu is found more often in use in the medical field (Huang 2002). Aside from phase transformation as a response to temperature, the transformation can also be induced by mechanical stress, a phenomenon called superelasticity (SE). In the austenite phase, under certain stress, the alloy can be deformed up to 10% and recover its original shape after the stress is removed (Duerig and Pelton 1994).

The applications of SMA devices in various fields are developed around the SME and SE properties. SE properties are normally used to form specialized structures for the human skeleton, oral devices in the medical field, or couplings and fasteners in the aero field. Based on SME properties, SMAs are more widely used as actuators, as in arterial intervention devices and surgical instruments in medicine; as switches, plugs, circuit breakers, and transmission controllers for industrial applications; and as MEMS devices and aircraft wings in the military and civil fields (Sreekumar et al. 2007).

2.1 Structure Design of SMA

The inspiration for soft robot design often comes from nature, where the objects of imitation are normally derived from hydrostatic skeletons, muscular hydrostats, or other bio-inspired designs. Most soft animals (such as worms or actinia) have no rigid skeletons and are composed of epidermis, muscle, body fluid, and neural systems. The hydrostatic skeleton is one typical structure, in which the muscle forms a closed cavity full of internal fluid. The fluid maintains a constant volume and when the longitudinal or circumferential muscle contracts, the body expands in a perpendicular direction (Quillin 1999). Different from arthropod animals, worms change their body stiffness by fluid pressure, muscle tension, and the compression of tissue (Trimmer and Issberner 2007) and they control muscle

contraction and expansion to achieve shape deformation and locomotion by creating traveling waves (Trueman 1975).

Many soft robots with hydrostatic skeletons have been developed based on SMA actuators. A constant volume design is a popular scheme that resembles the biological principle. Dario pioneered this kind of crawler robot (Menciassi et al. 2004), and the SoftBot that came after it is another typical case (Kate et al. 2008). It includes three main components: the silicone rubber body wall, the SMA spring actuator, and the control system. SMA coils are bonded inside the body wall and drive in a linear direction after heating, and the contoured body wall thickens and serves as the bias spring to supply the antagonistic force to the SMA actuator. Under the body wall is an inner compartment, and the space between the inner compartment and the body wall is sealed to allow transforming forces and regular stiffness with pressure. As shown in Fig. 1, by pulsed heating in each segment, the four SMA coils can adjust the contacts between the legs and the ground, creating a peristaltic posture that leads forward or crawls back. The force and contractions of the actuators are controlled by the heating frequency and duty cycle; a genetic algorithm was used to achieve more complex movement.

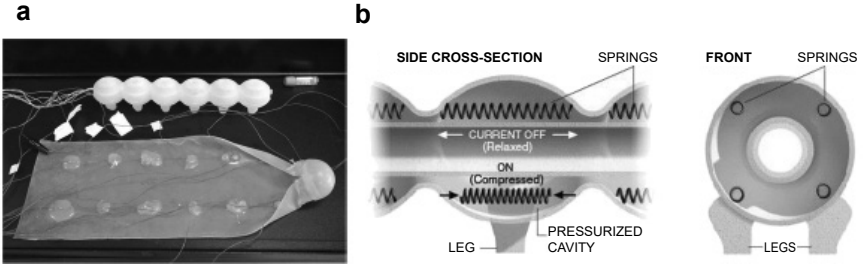

Figure 1. Soft-Bot. **(a)** Prototype of the Soft-Bot. **(b)** The model of the robotic caterpillar and its internal structure. Adapted permission from Dr. Barry Trimmer.

Different from the robot described above, the SMA actuator is set radially in the Meshworm robot (Kim et al. 2013), shown in Fig. 2. This is a constant length design that simulates *oligochaetes*. One segment of the robot body exhibits radial expansion, while the radial SMA coils contract in an adjacent segment, and the essential locomotion is derived from ground contact following the peristaltic wave. Linear potentiometers are set in each segment to detect the length change and provide close-looping control. Three control algorithms were analyzed to actualize lower energy consumption and a higher speed. Two longitudinal SMA coils were set on two sides of the body, and steering was incorporated into the motor ability. One important feature of a soft robot, low impedance to external pressure, is tested by hammer in this system.

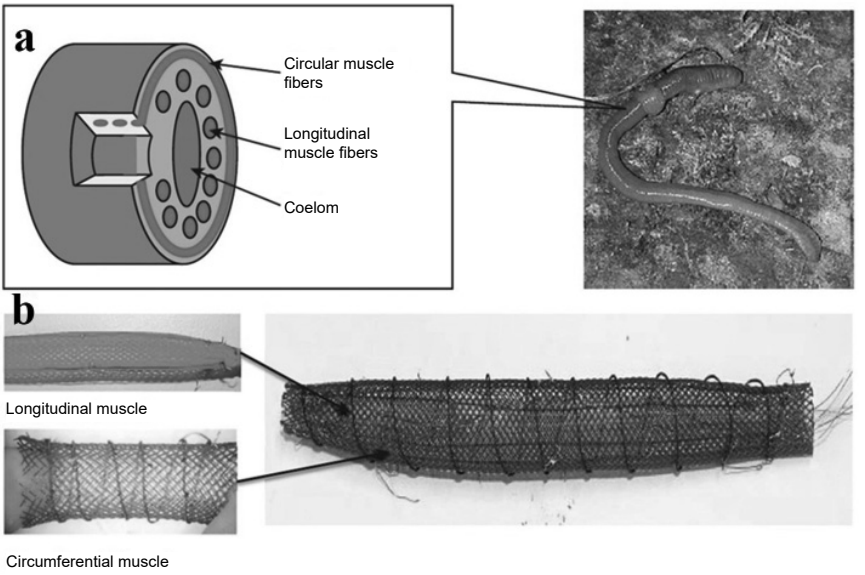

Figure 2. (a) Simulating the muscular structure of oligochaetes. **(b)** The Meshworm exhibits peristaltic locomotion by SMA actuators. Adapted with permission from ref. (Kim et al. 2013), copyright © Elsevier Publishing Group 2013.

The muscular hydrostatic structure is also without skeletal support, but unlike the case with a hydrostatic skeleton, it does not have a separate fluid cavity that is mainly composed of muscle tissue. The typical muscular hydrostatic structure is composed of transverse and longitudinal muscles, which always resist and work each other to apply vertical motion. The incompressible features of the muscle make it work similarly as fluid supplies pressure. Typical examples include the tongue, the elephant nose, and cephalopods.

Cephalopods are the most common objects whose motion is simulated, due to their intricate motion ability. Cephalopods can deform their shape to fill a narrow space, and the arms can apply complex manipulations. An octopus-inspired robot is always a hot topic for scientists (Zheng et al. 2014). An octopus arm has transverse, longitudinal, and oblique muscles that form a distinct structure that generates shortening, elongation, bending, or torsion (Kier and Stella 2007), as shown in Fig. 3a.

To develop octopus-inspired robots, one approach is to form the actuator system based on the real anatomy and mechanisms (Margheri et al. 2012), where the SMA actuator is always used to imitate the transverse, longitudinal muscles (Calisti et al. 2012, Mazzolai et al. 2012). As shown in Fig. 3b, a cylinder composed of plastic fiber braid and a silicone layer forms a robot arm with a highly deformable ability, and radial SMA

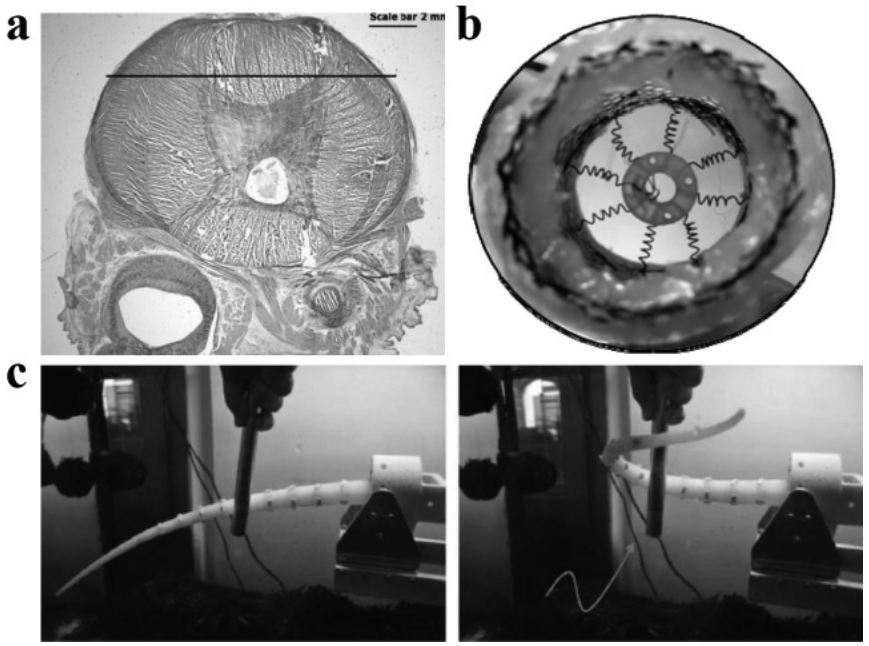

Figure 3. Octopus-inspired robot. **(a)** The cross-section morphology of the octopus arm. Adapted with permission from ref. (Margheri et al. 2012), copyright © IOP Publishing 2012. **(b)** The SMA springs inside the arm to achieve local actuation. **(c)** One soft robot arm wrapping around a bar. Adapted with permission from ref. (Mazzolai et al. 2012), copyright © IOP Publishing 2012.

coils are used to perform local deformations (Mazzolai et al. 2012). The arm was tested in the water for its wrapping ability and interaction with its surroundings, shown in Fig. 3c; it can bend, elongate, and shorten. The SMA actuator is also used to drive other bio-inspired soft robots, such as the Starfish-Like Soft Robot (Mao et al. 2014), the material characteristics make it a good choice to replace different muscles.

2.2 Controller of SMA

A SMA actuator is driven primarily by an electric heating current, and temperature control is the key to its implementation. These actuators are sensitive to changes in the environmental temperature and force load, both factors that can lead to the phase transformation of the materials and affect the driving performance. By studying the dynamics of the actuator, the phase transformation model and the convection heat transfer of SMA units, some open-loop control models have been established (Jala and Ashrafiuon 2006, Jayender et al. 2008). However, environmental changes result in

varying control accuracy, which creates a major challenge. Experiments have shown that with external feedback, close-loop control provides SMA actuators with high control accuracy and position feedback (Hadi et al. 2010) and force feedback (Teh and Featherstone 2008) are commonly used.

In recent years, the resistance feedback control of SMA actuators has received more attention. One problem with developing soft robots is that we currently have no general theory of how to control such unconstrained structures. In the SMA-actuated soft robot, in order to achieve precise control with continuous deformation, the combination of actuation and sensing is a possible solution. During phase transformation, the resistance value of SMA materials can show a significant change, 8%–15%, which is clearly more than can be accounted for by differences occurring solely due to the shape change. By establishing a descriptive mathematical model of the strain-resistance relationship of SMA, a self-sensing feedback model can be achieved to apply accuracy control to a SMA-actuated soft robot (Wang et al. 2012b). When it comes to the limits in complex SMA unit shapes, the resistance value of coils or other shapes is hard to describe, which is why current research tends to be limited to the SMA wire actuator.

Both the shape changing and the force generation of SMAs derive from temperature alternation, and the phase transformation of the SMA and the temperature has nonlinear relationship, as shown in Fig. 4. To achieve robust control, methodologies have been used to describe the nonlinear function, such as neural networks, iterative learning, or fuzzy control. After establishing the control scheme of the whole soft robot, engineers build the models based on the locomotive patterns of soft-bodied animals

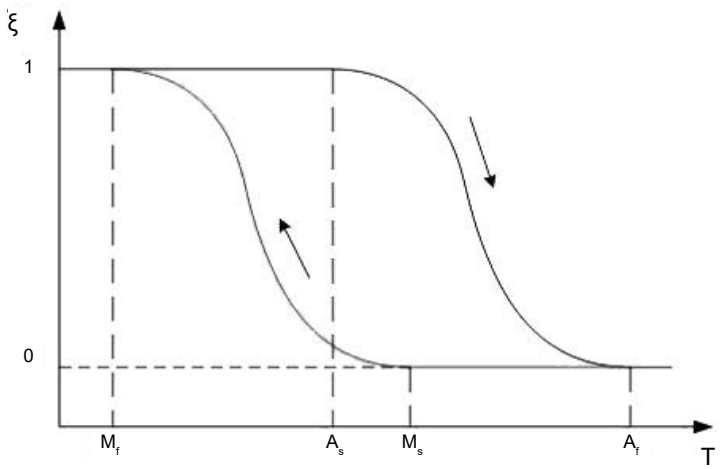

Figure 4. The hysteresis relationship of phase transformation and temperature for SMA actuators. Adapted with permission from Wikipedia.

and they consider the frequency, output force, and shape change mode of the corresponding SMA actuator to achieve motion schemes and to optimize efficiency. To control a SMA actuator for a soft robot, the technical combination of the material properties, the actuator design, and the feature extraction of the soft robot are all considered.

2.3 Fabrication of SMA

In most cases, when a SMA is used as the actuator for a soft robot driving system, the actuator is generally filamentous or in sheet form. SMA wires can deform along the axial direction or bend along the vertical direction, depending on the training process. Actuators with contraction along the axial direction are more widely used for significant larger outputs, and they can contract from heating and be extended under a bias force from another unit. To increase the deformation ratio, the SMA wires are sometimes wound into coiled springs, and in other cases, a linear shape is retained in order to supply a larger output.

For the SMA wire actuator, reciprocating motion can be achieved using different structures, for example, a passive bias force by spring (Lan and Yang 2009) or antagonistically paired wires (Teh and Featherstone 2008). In all these designs, the primary problems to be solved are slow response and cyclic degradation. The frequency of the SMA can be increased by a cooling system (Romano and Tannuri 2009) or repeat heating, with antagonistic actuation design being another option. Cyclical degradation is caused by the functional fatigue of SMA, where the material may lose its SME ability; this means that the driving displacement decreases with the cycle numbers. Experiments have shown that cyclical degradation can be improved with proper pre-straining and additional component design (e.g., spring and stopper).

In a soft robot actuator design, it is worth considering the use of soft materials with elasticity to work as additional components and to supply pre-straining to the SMA actuator to optimize the degradation property; in most cases, an antagonistic design demonstrates better function than a bias spring design. A SMA sheet actuator can provide more flexible motion based on different structure designs (Leester-Schadel et al. 2007), as shown in Fig. 5; the direction of motion can be vertical or can be along the tangent direction of the plane. The key properties such as deformation ratio and output force can also be varied by structural design.

A SMA sheet can be made by using several different processing methods, as in the shape deposition manufacturing (SDM) technology (Cho et al. 2009) shown in Fig. 6, as well as by laser cutting. One problem that needed to be solved for SMA actuators was how to embed the SMA into the soft materials; surface micromachining technology can be used

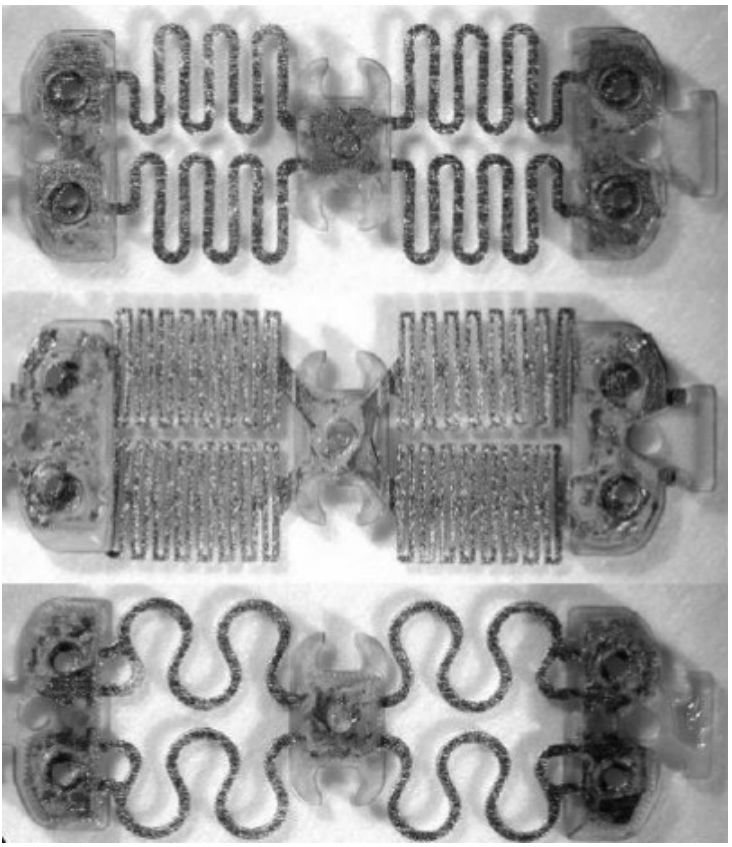

Figure 5. SMA actuators with different structure design. Adapted with permission from ref. (Leester-Schadel et al. 2007), copyright © SPIE 2007.

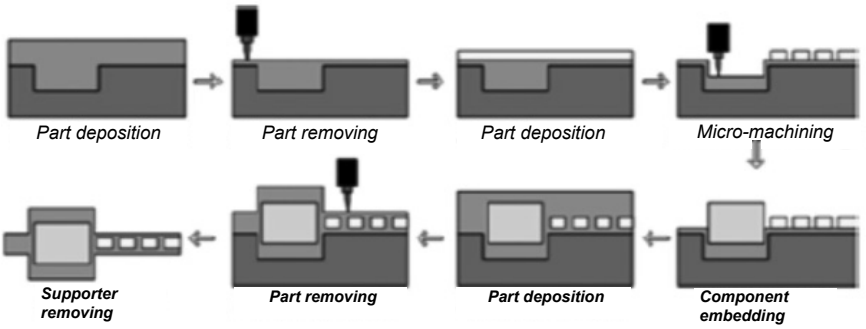

Figure 6. Schematic diagram of SDM process. Adapted with permission from ref. (Cho et al. 2009), copyright © Springer Publishing Company 2009.

to embed SMA wires into a 6 μm thick polyimide base (Kate et al. 2008). Previously, more processing was practiced to embed the SMA actuator into the robot body (Leester-Schadel et al. 2008), although a simple mechanical connection is still one popular option.

2.4 Brief Summary

Shape memory alloy actuators can be used widely as the driving element of a soft robot, due to their high mass-specific force. A general review of the material properties, structural design, and fabrication of SMA actuator is given in this chapter. The SME property of a SMA actuator makes it a suitable alternative to a muscle unit and by a multi-array of actuator settings, the system can achieve sophisticated motion. With the development of fabrication processes for SMA actuators and the use of embedding techniques, the bio structure design has become more flexible. Furthermore with the improvements of the self-sensing technology of the SMA actuator, more reliable and continuous control might be achieved in a soft deformation in the future. The design principle of the SMA actuator in soft robots will tend to show more complex morphological changes to simulate the muscle movement of soft animals by advanced fabrication. In addition the SMA might be used more frequently as a sensor in the bio-structure to achieve its self-sensing property.

3. Stretchable Elastomeric Sensor for Soft Robotics

Sensors are essential for robots to interact with the world. This is exacerbated in the field of soft robotics, where manipulating deformable and delicate objects is something that conformal and flexible soft robots are more adapted to do compared to traditional hard-bodied robots. Unlike in hard-bodied robots, the sensors used in soft robotics must be soft in order to keep the entire system completely flexible and stretchable. Although small rigid elements could still be cast inside a soft system, problems often appear at the interface between stiffness gradients and can lead to failure.

Soft sensors can be used typically to measure the curvature of a leg on a soft robot (Fig. 7a, Shepherd et al. 2011) or if there is a contact between a soft gripper and an object (Fig. 7b, Ilievski et al. 2011). In addition to soft-bodied robots, soft sensors can also be very useful for joint angle measurements on the human body (e.g., for motion tracking). As their high conformability reduced the shear on the skin, the sensors are very comfortable to wear and allow measurements without any impact on the user.

Several approaches can be used to fabricate sensors that are flexible and stretchable (Park et al. 2015). One strategy is to use regular conductive

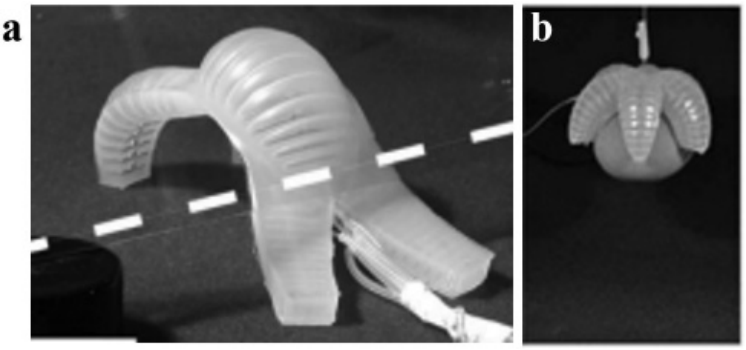

Figure 7. (a) A multi-gait soft robot. Adapted with permission from ref. (Shepherd et al. 2011), copyright © the National Academy of Sciences 2011. **(b)** Soft gripper lifting an egg. Adapted with permission from ref. (Ilievski et al. 2011), copyright © WILEY-VCH Verlag GmbH & Co. KGaA, Weinheim 2011.

materials such as metals or semiconductors, make them thin enough to allow them to bend and cut a meander pattern to allow them to stretch like a spring. An example of such stretchable electronics (Kim 2011) is commercialized by the company MC10 (Fig. 8), where ultra-thin, skin mounted sensors provide personalized biofeedback to the user. Although sensors fabricated using this approach can conform to most of the skin

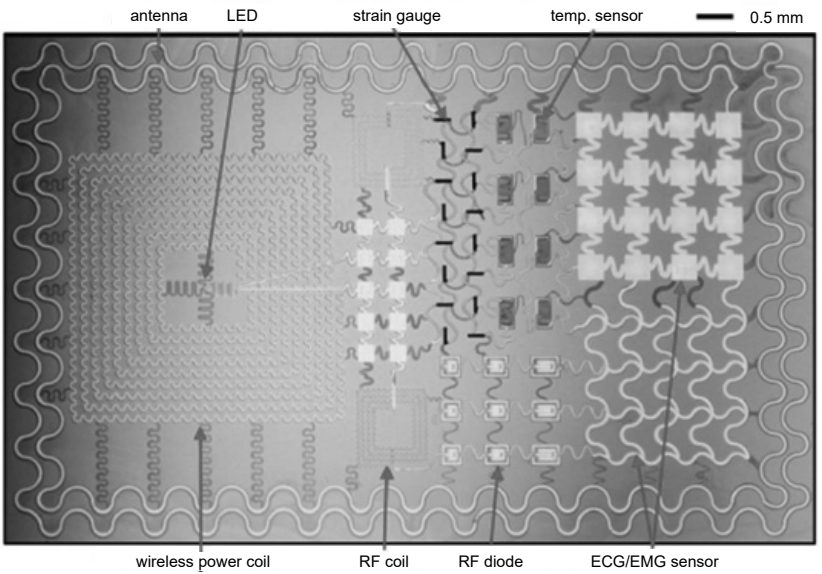

Figure 8. Epidermal electronics, commercialized by the company MC10. Adapted with permission from ref. (Kim 2011), copyright © The American Association for the Advancement of Science 2011.

on the human body, it is unable to conform to the high strains (> 100%, Menguc et al. 2014) that are experienced on joints such as on the elbow or the knee.

Another approach is to use only soft or liquid state materials. Indeed, many elastomers offer a high stretchability until failure (> 900%, Smooth-on) while maintaining a low shore hardness (lower than 1A). By using well known techniques from microfluidics, it is possible to pattern microchannels inside the rubber and fill them with a conductive liquid. It is also possible to use other approaches to pattern liquid metals on surfaces (Joshipura et al. 2015). By reading the change in resistance as the sensor is stretched, one can calibrate a change of the electrical resistance as functions of the strain, normal pressure and other features that will be described in the following chapter. Other soft sensing techniques using capacitance (Fassler and Majidi 2013, Frutiger et al. 2015, Lipomi et al. 2011, Sun et al. 2014) or optic (Kadowaki et al. 2009) measurements are well studied, however, they are not covered in this chapter.

3.1 Design and Modeling of Stretchable Sensor

Soft sensors are designed primarily to provide information under strain as well as pressure. This design can nevertheless be modified to provide other kinds of information, such as curvature (Majidi et al. 2011) or shear (Vogt et al. 2013) on the surface. It can also be modified to combine modalities, such as sensing strain and normal pressure simultaneously (Park et al. 2012). The conductive liquid, with a resistivity ρ, plays an important role in the functionality of the soft sensor. One type of conductive liquid that is used is an ionic liquid (Cheung et al. 2008), which requires an alternating voltage to read a change of electrical resistance to avoid the electrolysis of the fluid. Another option is to use a mixture of conductive particles (such as carbon nanotubes (Yamada et al. 2011), carbon grease (Muth et al. 2014), etc.) and a carrying medium (e.g., grease or oil). However, the latter option presents the disadvantage that the percolation network between the particles is strongly altered under high deformation, resulting in strong peaks followed by decay in the electrical resistance reading (Muth et al. 2014), as shown on Fig. 9. This effect also alters the sensor's repeatability. Finally, the sensor's initial electrical resistance is relatively high (> kΩ).

In this chapter, the presented soft sensors use eutectic Gallium Indium (eGaIn, Fig. 10) as a conductive liquid. Because it is a metal which is liquid at room temperature, eGaIn presents ideal electrical properties ($\rho = 29.4 \times 10^{-6} \Omega/\text{cm}$, Chiechi et al. 2008). Compared to other conductive liquids, it nevertheless has a very high surface free energy (ca. 630 dynes/cm).

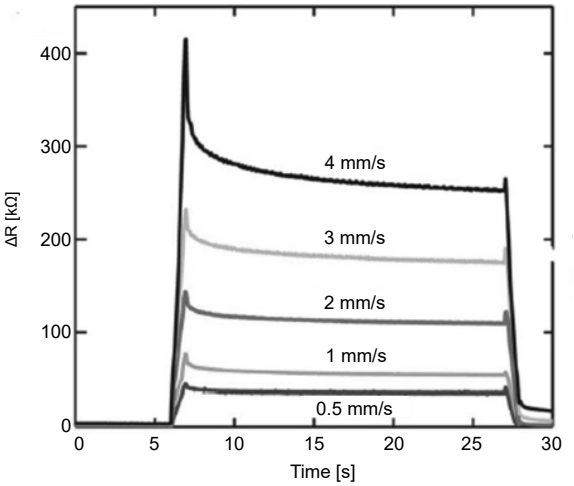

Figure 9. Step response for 3d-printed sensors for different printing speeds. One can notice peaks and decay due to the use of carbon grease as a conductive medium. Adapted with permission from ref. (Muth et al. 2014), copyright © John Wiley and Sons Company 2014.

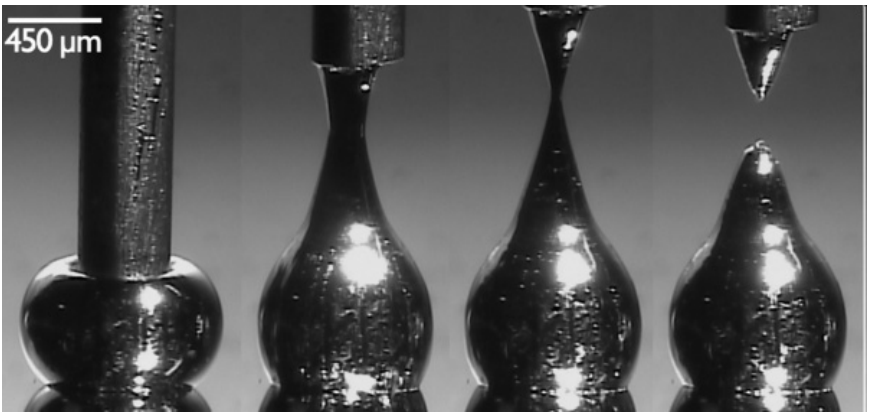

Figure 10. Eutectic Gallium Indium (eGaIn). Adapted with permission from ref. (Chiechi et al. 2008), copyright © John Wiley and Sons Company 2007.

The simplest sensor design is a single microchannel of length L, width w and height h. The microchannel is filled with a conductive liquid of resistivity ρ. The overall resistance, R, measured at both ends is equivalent to:

$$R = \rho \frac{L}{wh} \tag{3-1}$$

When strain is applied to the soft sensor, the overall length of the micro-channel will increase and the overall cross-section will decrease as shown in Fig. 11a (left).

Equation (3-1) then becomes:

$$\Delta R = R - R_0 = \rho \frac{L + \Delta L}{(w + \Delta w)(h + \Delta h)} - \rho \frac{L}{wh} \tag{3-2}$$

Since $\epsilon = \frac{\Delta L}{L}$, one can replace Δw by $-v\epsilon w$ and Δh by $-v\epsilon h$. With a typical Poisson's ratio v of 0.5 for elastomers, equation (3-2) can then be simplified to:

$$\Delta R = \frac{\rho \varepsilon L(8 - \varepsilon)}{wh(2 - \varepsilon)^2} \tag{3-3}$$

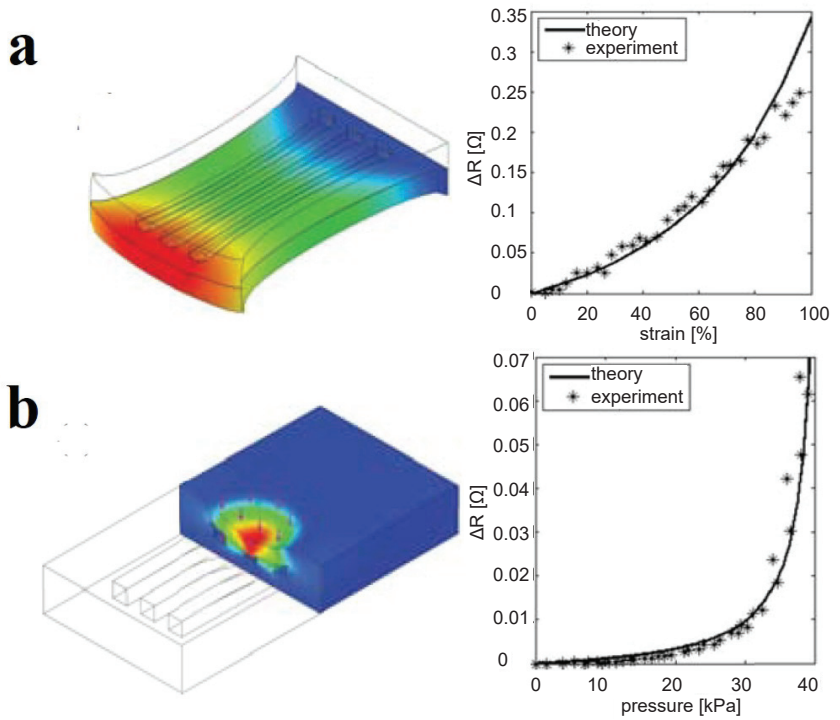

Figure 11. Simulation and experimental results on soft sensor. **(a)** Soft sensor response to strain. **(b)** soft sensor response to normal pressure. Adapted with permission from ref. (Park et al. 2012), copyright © IEEE 2012.

Figure 11a (right) shows the experimental and theoretical relationship between strain and electrical resistance change for a single microchannel.

Under normal contact pressure p of a microchannel, the overall length of the microchannel does not change, but its width and height will be decreased locally (Fig. 11a, left). With the assumption that the cross-section of the microchannel is square and E is the elastic modulus of the elastomer material, equation (3-1) becomes:

$$\Delta R = \frac{\rho L}{wh}\left\{\frac{1}{1-2\left(1-\nu^2\right)wp/Eh}-1\right\} \tag{3-4}$$

A comparison between the theoretical and experimental values is shown in Fig. 11b (right).

Without going into details, the micro-channel configuration can also be designed to sense other modalities such as curvature (Majidi et al. 2011) or shear (Vogt et al. 2013). Finally, it is also possible to measure several modalities simultaneously (Park et al. 2012) such as normal pressure and strain.

3.2 Fabrication and Characterization of Stretchable Sensor

In this section, the fabrication of a soft sensor is explained in detail. This soft sensor has been designed to be used on a wrist angle sensing band shown in Fig. 12 (Vogt and Wood 2014). It is primarily designed to measure strain, but will also be sensitive to normal pressure. Its overall dimensions are 45 × 15 × 0.7 mm. The main fabrication steps are shown in Fig. 13.

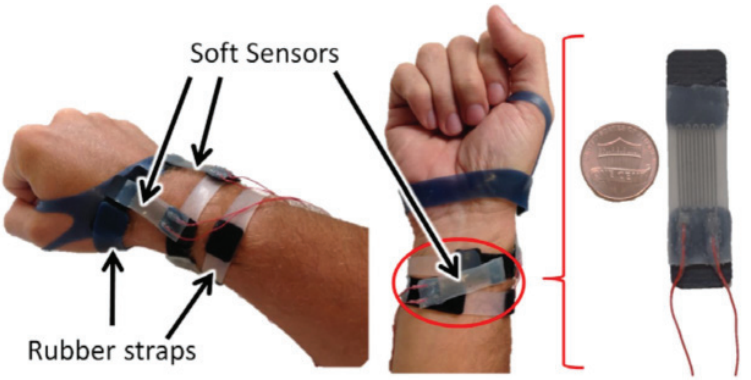

Figure 12. Wrist angle measurement using soft sensors. Adapted with permission from ref. (Vogt and Wood 2014), copyright © IEEE 2014.

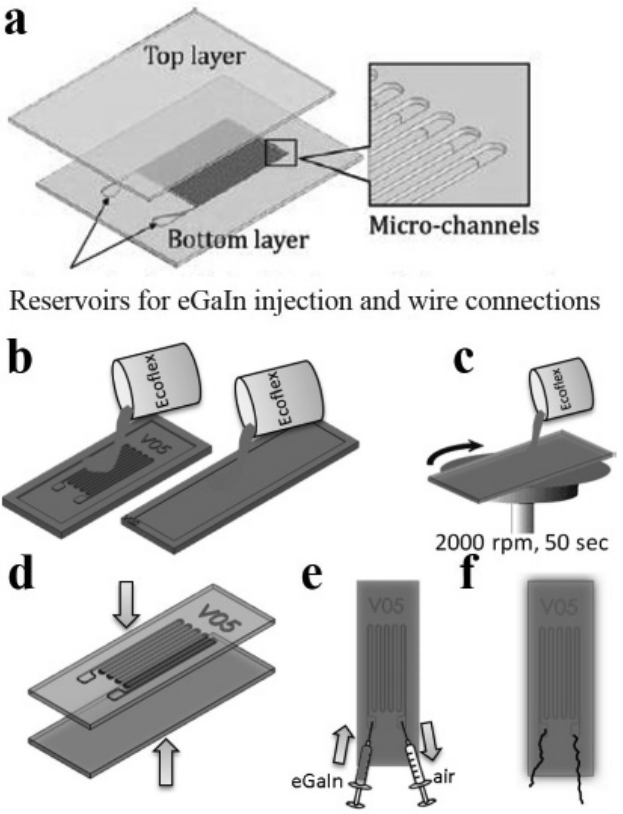

Figure 13. Main fabrication steps for soft sensors. **(a)** The schematic design of two molds. The top layer is flat and the bottom one contain the negative of the microchannel's design. **(b)** Schematic of pouring elastomers into the molds. The trapped air bubbles are evacuated by placing the molds in a vacuum for ten minutes. **(c)** Bonding two layers together by spin-coating a thin uncured wet layer of the same material on the surface of the flat layer. **(d)** Laying one layer over the other during bonding operation. It is important not to trap any air bubbles. **(e)** Filling Gallium Indium (eGaIn) into the mold. One syringe is used to inject eGaIn and the other one to remove air from the microchannels. **(f)** Connecting the soft sensor to an electronic readout circuit. Adapted with permission from ref. (Vogt and Wood 2014), copyright © IEEE 2014.

The first step is to design the molds with a CAD software such as Solidworks©. Two molds will be required. One will be flat, and the other one will contain the negative of the micro-channel's design.

The micro-channel cross-section size depends mostly on the technique to create the mold. Using an Objet 30 Scholar[1] 3D printer, a typical cross-section dimension is 300 × 300 mm. By using other mold fabrication techniques

[1] Objet 30, Stratasys, Eden Prairie, MN 55344, USA.

such as soft lithography, one can get micro-channel dimensions under 100 × 100 mm. By increasing the number of micro-channel loops one will increase the sensitivity of the soft sensor. In this example, the micro-channels are looped nine times to connect both extremities. At each extremity, reservoirs are added to ease the filling and wiring that will be described later. Depending on the mold fabrication technique, an additional step is required before pouring elastomer into the mold for the first time. 3D printed molds must be baked at 60ºC for at least seven hours, to help dry the mold and prevent the elastomer from not curing properly when in contact of the mold. When using molds fabricated using soft lithography, it is necessary to silanize the wafer to prevent the elastomer from sticking to the surface of the molds once cured. This is done by placing the wafer in a vacuum chamber containing a recipient with a few drops of Trichloro (1H,1H,2H,2H-perfluoroctyl) silane[2] for more than three hours.

The next step is to pour elastomers into the molds (Fig. 13b). Elastomers are provided typically in a two part mixture and a planetary centrifugal mixer such as the Thinky © Mixer[3] offers the best mixing results. The elastomer used in this example will be Ecoflex® 00-304 as it offers a low shore hardness 00-30 and a high elongation at break (900% Smooth-on).[4] Another typical silicone rubber used for soft sensors is PDMS Sylgard 184.[5] This elastomer has a higher shore hardness than Ecoflex, but has the advantage of being able to bond layers together using oxygen plasma surface treatment. After pouring either of these elastomers, the next step is to place the molds in a vacuum for ten minutes to allow trapped air bubbles to evacuate. The molds can then be placed in an oven at 60°C to accelerate the curing (~ 20 min) or be left at room temperature for at least four hours.

Once both layers are cured, the next step is to bond them together. In the case of Ecoflex 00-30, this is done by spin-coating (2000 rpm, 50 sec) a thin uncured wet layer of the same material on the surface of the flat layer (Fig. 13c). The flat layer with the thin wet layer is then placed in an oven at 60°C for ~ 50 seconds to slightly cure the wet layer. If this step is omitted, the microchannels may be filled by capillary action when both layers are bonded together. On the other hand, if the flat layer is left too long in the oven, there is a risk that the wet layer will cure too much and the bonding will be very weak. When bonding both layers (Fig. 13d), it is important to not trap any air bubbles when laying one layer over the other. The soft sensor can then be left for curing for at least four hours at room temperature.

Once both layers are bonded together, the soft sensor is ready to be filled with eutectic Gallium Indium (eGaIn). Two syringes are required to

[2] Sigma Aldrich.
[3] Thinky Mixer ARE-310, Thinky USA, Laguna Hills, CA 23151, USA.
[4] Smooth-On Inc., Easton, PA, 18042, USA.
[5] Dow Corning, Midland, MI.

do this, one to inject the eGaIn, and the other to remove the air from the microchannels to ease the injection as shown in Fig. 13e. It is recommended to first inject air in one of the reservoirs to make sure that the microchannels have not been filled by capillary action. This will also facilitate the placement of the needle on the other reservoir for the syringe containing eGaIn. The air can then be removed and the eGaIn injection can start. It is recommended to tilt the syringe containing eGaIn slightly so as to not inject any air in the micro-channels which will result in an open circuit.

The last step is to insert wires (Fig. 13f) to be able to connect the soft sensor to an electronic readout circuit. It is recommended to use a small wire (e.g., 18 AWG) and to solder one extremity to the core of a 22 AWG solid core wire (~ 2 mm long). This will help anchor the wire in the reservoir. Once soldered to the core, the wire can be inserted into the soft sensor's reservoir following the hole created by the needle during the injection. To improve the sensor's robustness, a silicone adhesive such as Sil-Poxy®[6] can be used to glue the wires onto the soft sensor's surface.

To test the soft sensor, the easiest way is to connect it to an ohm-meter. Depending on the microchannel's design, the initial resistance should be a few ohms and a significant difference should occur when the soft sensor is stretched or compressed. Common issues can be the delamination of both layers, air injected in the microchannels, bad contact between the wire and the eGaIn in the reservoir, etc. Under strain, the higher stress concentration generally happens at the transition between soft and hard materials, in this case between the soft sensor's surface and the wire.

3.3 Brief Summary

In this chapter, a general overview is given about the theory and design of soft sensors which are essential for soft systems in order to interact with the world. In addition to do sensing on soft robots, soft sensors also have an important potential to be worn on the human body for motion tracking (Menguc et al. 2014, Vogt and Wood 2014). Compared to other soft sensing technologies, the main advantage of using a soft elastomer containing microchannels filled with a conductive liquid is to reach very high levels of elasticity and conformability.

4. Ionic Polymer-Metal Composite for Soft Robotics

Ionic Polymer Metal Composites (IPMCs) are innovative materials made of an ionic polymer membrane with plated gold as electrodes on both sides

[6] Smooth-On Inc., Easton, PA, 18042, USA.

chemically (Shahinpoor and Kim 2001, Shahinpoor and Kim 2005), which can serve as an alternative actuator as well as sensor for soft robotics. See Fig. 14a. The most interesting characteristics of IPMC are its softness and lightness; moreover, when a electric field is applied across the thickness of

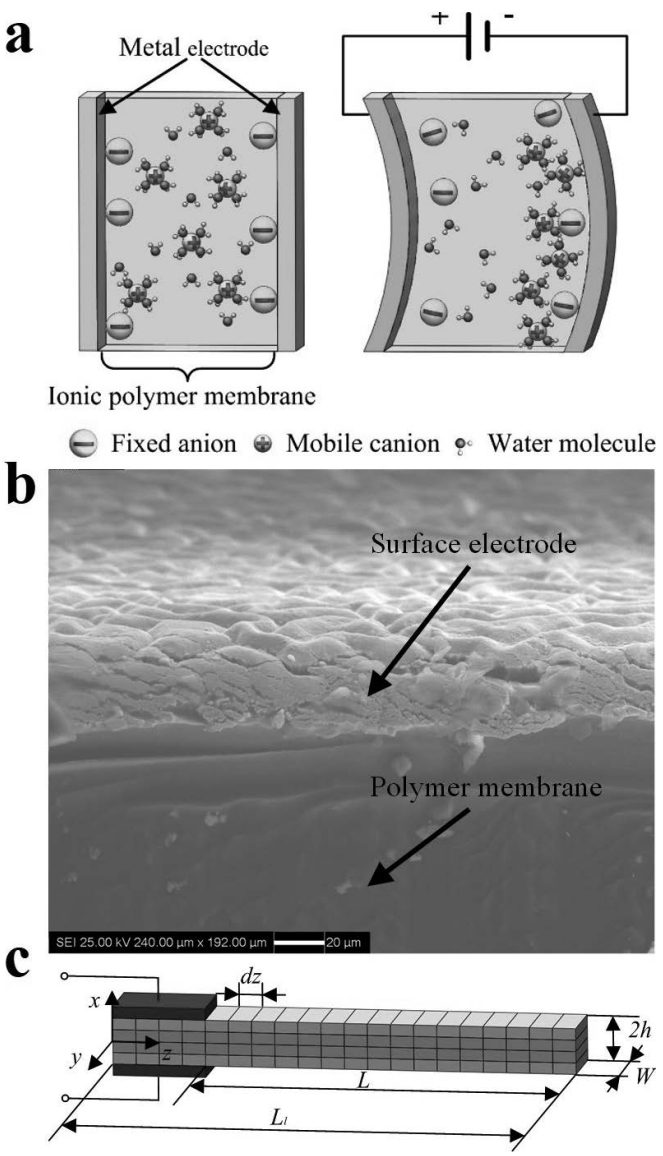

Figure 14. Physical and computation model for IPMC. **(a)** Illustration of IPMC operating principle. Adapted with permission from ref. (Shen et al. 2013), copyright © InTech 2013. **(b)** SEM image of IPMC cross-section. **(c)** Schematic of IPMC beam. Original figures.

direction, the IPMC would perform deformation. On the other hand, they generate a detectable voltage if subjected to a mechanical deformation. Briefly, it has the advantages of low activation voltage actuation (1-2V), limited power consumption, low noise, and high flexibility. Therefore the ionic polymer metal composite provides the possibility for developing a low-noise, micro-size, soft biomimetic robot.

4.1 Design and Modeling of IPMC

Several works concerning the modeling of IPMC have been reported. The influence of the electrode conductivity on the transduction behavior of IPMC was previously investigated by Shahinpoor and Kim (Shahinpoor and Kim 2000). Another model that describes electromechanical transduction in relation to the electrostatic interaction within the polymer was proposed by Nemat-Nasser and Li (Nemat-Nasser and Li 2000). The electrical dynamics of the IPMC based on Nemat-Nasser's work was elucidated by Chen and Tan (Chen and Tan 2008). Porfiri and his co-workers showed that the electrodes do affect the charge dynamics significantly and hence the actuation performance of IPMC (Porfiri 2009). An electrode model for IPMCs based upon a structural formation of electrode materials was proposed by Kim et al. (Kim et al. 2007).

The physical based model combines the effect of the electrode resistance change and the charge dynamics of the ionic polymer. Figure 14b shows the Scanning Electron Microscope (SEM) image of IPMC cross-section. The surface electrode and the inner polymer membrane composite of the IPMC. The length and width of the IPMC beam is L and W. The thickness of the polymer membrane and electrode are $2h$ and h_e. The unit length of the curved IPMC midline is assumed as dz. The unit cell length of the stretched electrode can be expressed as (Shen et al. 2014):

$$dL\left(\hat{h}, w(L,t)\right) = d\gamma\left(w(L,t)\right)\left(r\left(w(L,t)\right) + h + \hat{h}\right) \tag{4-1}$$

where $\gamma(t)$ is the angle of the curved beam, $r(w(L, t))$ is the radius of the midline and $\hat{h}$ is the position of the unit cell along the thickness direction of the electrode. The expressions of $\gamma(t)$ and $r(w(L, t))$ are defined in ref. (Kim et al. 2007). The reciprocal of the electrode resistance is expressed as follows (Shen et al. 2014):

$$\frac{1}{R_e\left(w(L,t)\right)} = \int_0^{h_e} J_e \frac{(1-P_x)}{\left(r\left(w(L,t)\right)+h+\hat{h}\right)}\frac{d\hat{h}}{a} + \int_0^{h_e} \frac{P_x r(w(L,t))}{G_e\left(r\left(w(L,t)\right)+h+\hat{h}\right)L/W}\frac{d\hat{h}}{a}$$

$$= \left[J_e\frac{(1-P_x)}{a} + \frac{P_x W r(w(L,t))}{G_e a L}\right]\ln\left(\frac{r\left(w(L,t)\right)+h+h_e}{r\left(w(L,t)\right)+h}\right) \tag{4-2}$$

with

$$J_e = \frac{(1-P_y)W}{E_e L} + \frac{P_y W r(w(L,t))}{G_e L},\ E_e = F_e \frac{(1-P_z)}{r(w(L,t))} + G_e \frac{P_z}{r(w(L,t))},$$

$$F_e = \frac{\rho_p (a-2s_v)}{a^2} + \frac{2\rho_p \rho_v s_v}{2\rho_p s_v^2 + \rho_v (a^2 - 2s_v^2)},\ G_e = \frac{\rho_v (a-s_v)}{a^2} + \frac{\rho_p \rho_v s_v}{2\rho_p s_v^2 + \rho_v (a^2 - 2s_v^2)},$$

where ρ_p and ρ_v are the resistivity of the particle and void, a and s_v are the side length of the unit cell and void cube, P_x, P_z, P_z are the percentages of the defective cube in the x, y, z direction. By inversing (4-2), the expression of the resistance of the electrode can be obtained.

Analytical solutions are available for several special cases of geometric nonlinearity in a cantilever beam. Herein, the finite element approach is used to describe the dynamics of the IPMC strip. The IPMC actuator was assumed to be divided by a series of elements, where the voltage on each element is constant, as shown in Fig. 14c. The Nernst-Planck equation describes the cation migration and diffusion in the polymer element backbone as (Nemat-Nasser and Li 2000)

$$\frac{\partial C}{\partial t} + \nabla \cdot (-D\nabla C - \hat{z}\mu F C \nabla \phi) = 0 \tag{4-3}$$

where $C, t, \mu, D, F, \hat{z}$ and ϕ are the cation concentration, time, mobility of cations, diffusion constant, Faraday constant, charge number, and electric potential in the polymer element respectively. The ions move within the matrix of the polymer. The local charges will concentrate at the boundary between the polymer and surface electrodes. As a result, an electric field will increase in the opposite direction. The Poisson's equation describe the process as

$$\nabla \cdot \vec{E} = -\nabla^2 \phi = \frac{\rho}{\hat{\varepsilon}} \tag{4-4}$$

where $\hat{\varepsilon}$ and $\vec{E}$ are the absolute dielectric constant and strength of the electric field respectively. ρ is the charge density and is defined as

$$\rho = F(C - C_0) \tag{4-5}$$

where C_0 is the constant anion concentration. The time variable of $\rho(x, z, t)$ can be transformed in the Laplace form. The expression in the Laplace domain can be obtained as (Shen et al. 2014)

$$\rho(x,z,s)s - D\frac{\partial^2 \rho(x,z,s)}{\partial x^2} + \frac{\hat{z}\mu F^2 C_0}{\hat{\varepsilon}}\rho(x,z,s) = 0. \tag{4-6}$$

Nemat-Nasser and Li presented a theory that the charge density at the boundary of polymer is proportional to the induced stress σ4 and is expressed as

$$\sigma(\pm h,z,s)=\alpha\rho(\pm h,z,s). \tag{4-7}$$

The boundary condition of (4-7) is $\rho(h,z,s) + \rho(-h,z,s) = 0$. The ionic flux in the x direction within the polymer is expressed as (Shen et al. 2014)

$$f(x,z,s)=-D[\frac{1}{F}\frac{\partial\rho(x,z,s)}{\partial x}-\frac{FC_0}{RT}E(x,z,s)] \tag{4-8}$$

where R is the gas constant, and T is the absolute temperature. The boundary condition of (4-8) is expressed as

$$f(h,z,s)=f(-h,z,s)=0. \tag{4-9}$$

By solving (4-9) and with the condition of $E(\pm h,z,s) \neq 0$, the expression of ionic flux can be obtained. Based on Ramo-Shockley theorem, the local current density at an electrode boundary is expressed as

$$j(z,s)=\frac{1}{h}\int_{-h/2}^{h/2}f(x,z,s)dx. \tag{4-10}$$

The electric potential on the surface of the IPMC element can be expressed as

$$\phi(\pm h,z,s)=\pm\frac{V(s)}{2}\mp\int_0^z j(z,s)W_e h_e R_e\left(w(L,s)\right)\frac{dz}{L} \tag{4-11}$$

where $V(s)$ is the voltage applied to the clamp. With (4-10) and (4-11), the expression of $\rho(x,z,s)$ is derived. By relating the induced stress $\sigma(\pm h,z,s)$ to the bending moment, one can obtain

$$\sigma(\pm h,z,s)=\frac{\pm hM(z,s)}{I} \tag{4-12}$$

where I is the moment of inertia of the IPMC element and $I = 2/3Wh^3$. With (4-7), (4-11) and (4-12), the bending moment can be obtained. With the linear beam theory, the tip displacement of the IPMC beam element relating to the z can be denoted as

$$\frac{d^2w(z,s)}{dz^2}=\frac{M(z,s)}{YI} \tag{4-13}$$

where Y is the Young's modulus. The angle of the curved beam element is donated as

$$\tan d\varphi(z,s)=\frac{dw(z,s)}{dz}. \tag{4-14}$$

By integrating the tip displacements of the elements, one can obtain the deformation of the IPMC as

$$w(L,s) = \int_0^L dz \left(d\varphi(z,s) + \frac{d\varphi(z,s)}{dz} \right). \tag{4-15}$$

Solving (4-15) with boundary conditions $w(0,s) = 0$ and $\frac{dw(0,s)}{dz} = 0$, the deformation of the IPMC $w(L,s)$ under the voltage $V(s)$ can be obtained. The actuation bandwidth of an IPMC actuator is relatively low (under 10 *Hz*). To accommodate the vibration dynamics of the beam, we project $w(L,t)$ on the first mode of vibration expressed as

$$X_1(z) = ch\beta_1 z - \cos\beta_1 z - \frac{ch\beta_1 L + \cos\beta_1 L}{sh\beta_1 L + \sin\beta_1 L}(sh\beta_1 z - \sin\beta_1 z) \tag{4-16}$$

where β_1 is the constant in relative with the natural frequency and the damping ratio. The actual tip displacement of the IPMC beam can be expressed as

$$w_l(L,t) = w(L,t)X_1(L). \tag{4-17}$$

4.2 IPMC as Actuator for Fish-inspired Soft Underwater Robot

The actuation effect of IPMC is induced by the transport of hydrated cations and water molecules and the associated electrostatic interactions within the polymer membrane. Thus, the IPMC can work directly in water without waterproof processing. With the advantages of high flexibility, low drive voltage, and large bending deflection, IPMC is one of the promising advanced materials for micro biomimetic underwater propulsion (Shen et al. 2013). It should be noted that according to previous work, when compared to a rigid flapping foil, the thrust efficiency of a two-dimensional flapping foil with chord-wise flexibility is experimentally shown to increase significantly, i.e., up to 36% (Prempraneerach et al. 2003).

Several pioneering works concerning the IPMC actuated underwater robots have been reported. Tan and his group presented the speed model for an IPMC-propelled robotic fish (Chen et al. 2010, Mbemmo et al. 2008). Porfiri and co-workers developed a modeling framework for the surge, sway, and yaw motion predicting biomimetic underwater vehicles propelled by IPMC and investigated the IPMC beam's hydrodynamics using numerical computation and digital particle image velocimetry (DPIV) (Abdelnour et al. 2009, Aureli et al. 2010, Peterson et al. 2009). Kim proposed an analytical model of IPMC actuator dynamic characteristics, which can be used for modeling a single- or multi-segment IPMC actuator that operates in

water (Yim et al. 2007). An efficiency model of a robotic fish was proposed, where the total power consumption of IPMC was considered in the model (Wang et al. 2012a). To study the robotic swimmer's thrust performance in micro-scale, an important dimensional parameter of fish, the Reynolds number Re, is introduced and is defined as

$$\mathrm{Re} = UL_f / v \tag{4-18}$$

where L_f is the fish length, U represents the steady swimming speed under the freely swimming condition, and v denotes the fluid kinematic viscosity. The Reynolds number of the robotic swimmer is low when its size is reduced. One could reduce the Reynolds number by increasing the kinematic viscosity of the fluid.

The robotic swimmer prototype consists of the rigid body shell, the soft IPMC stripe and the plastic tail fin, as shown in Fig. 15. It had a total length of 47.5 mm without the tail, 14.5 mm in height and 12 mm at its widest point. Its total weight approximated 5.05 g.

The hydrodynamic experiments were conducted in a horizontal low-velocity servo towing system with force detection apparatus on it. Figure 16 shows the mechanical components of the self-propelled experimental apparatus. The water tank, was filled with the mixture of water and glycerin. The force T_1, T_2 (see Fig. 16) was measured by the force transducers. The external force T_{ext} from the external apparatus acting on the swimmer can be measured by $T_{ext} = (T_1 - T_2)/100$.

Hydrodynamic experiments were performed to study the self-propelled speed and thrust force of IPMC swimmer. The robotic swimmer propelled

Figure 15. Prototype of the robotic swimmer. Adapted with permission from ref. (Shen et al. 2013), copyright © IOP Publishing 2013.

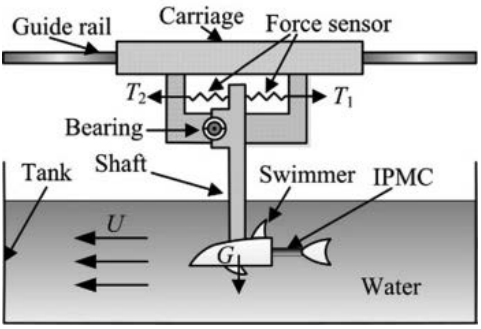

Figure 16. Illustration of experimental apparatus. Adapted with permission from ref. (Shen et al. 2013), copyright © IOP Publishing 2013.

by the IPMC tail swam freely in a tank, and its motion was recorded by a camera, which was set on top of the tank. A signal generator with a power amplifier provided the IPMC actuator sinusoidal signals. The captured images were analyzed. The velocities of the robotic swimmer were measured. Figure 17 shows the consecutive snapshot of the swimmer swimming in the tank.

The swimmer was towed under the servo towing system in the cruising speed measured above. For each cruising speed U_{exp}, the IPMC was under corresponding sinusoidal wave voltage input. According to the Newton's law, the robotic swimmer was considered to swim freely without the external force from the apparatus above acting on it, where the drag force F_D equals

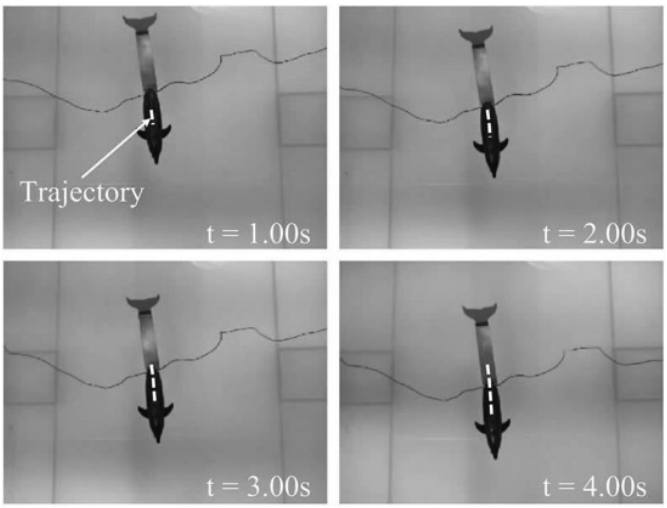

Figure 17. Consecutive snapshot of robotic swimmer in water. Adapted with permission from ref. (Shen et al. 2013), copyright © IOP Publishing 2013.

to the thrust force T_{exp}. When the robot swam under the speed U_{exp}, one could gain T_{exp} by measuring the drag force F_D. To obtain the drag force F_D, the input voltage of IPMC was set zero. Through towing the swimmer under the system at U_{exp}, the F_D was measured.

Figure 18 shows the experiment setup for the image capturing. The IPMC beam was fixed at one end and submerged in the fluids. A camera was set on top of the IPMC for the frame acquisition. Background lighting was turned off during testing while a spotlight was directed towards the reflective dots in order to increase the image contrast. The image analysis of the captured frames was performed.

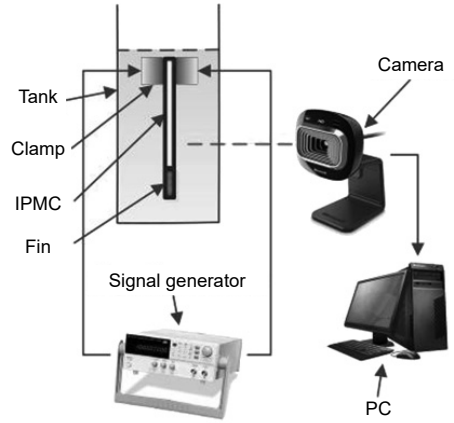

Figure 18. Schematic view of the image capturing apparatus. Adapted with permission from ref. (Shen et al. 2013), copyright © IOP Publishing 2013.

To measure the power consumption, the IPMC tail oscillated in the fluids under corresponding voltage input. The tip displacement s_f was measured through image processing. Then, the IPMC tail oscillated in air under the same voltage input and we measured the tip deflection s_a. The blocking force, F_b, of a cantilevered IPMC actuator can be written as (Lee et al. 2005)

$$F_b = \frac{3WHEd}{8L}V \tag{4-19}$$

with

$$d = \frac{2s_a H^2}{3L^2 V},$$

where W, H, L are the width, thickness and length of the IPMC beam respectively, V is the input voltage and E is the Young's modulus. The amplitude of the tail is far smaller than its length scale, so that the tail is

supposed to bend periodically at the tip. The average power that the IPMC output in the fluid during one cycle at frequency f can be obtained as

$$\begin{aligned}\overline{P}_{exp} &= \overline{P}_a - \overline{P}_f = \frac{\int_{t_s}^{1/f+t_s} F_b ds_a - \int_{t_s}^{1/f+t_s} F_b ds_f}{1/f} \\ &= \frac{fWH^3 E \int_{t_s}^{1/f+t_s} s_a \left(ds_a - ds_f\right)}{4L^3}\end{aligned} \tag{4-20}$$

where t_s is a random time point during IPMC tail performing, $\overline{P}_a$ and $\overline{P}_f$ are the power consumption of IPMC in air and fluid respectively.

Figure 19a-d shows the experimental results of swimmer velocities. At low viscosity, the optimal frequency for the speed approximated 1 *Hz*. When the viscosity increases, the optimal frequency for the speed decreases. The speed of the IPMC swimmer rises with the increasing of voltage amplitude, as shown in Fig. 19a and b. By comparing the experimental results of tail 1 and tail 2, one can find that the velocity of tail 2 is generally higher than that of tail 1. This means that the speed can be improved by increasing the voltage amplitude as well as the size of IPMC. It should be noted that as the viscosity rises, its velocity has a significant decrease, which is shown in Fig. 19c and d. The results also show that the robotic swimmer has relatively low speed at low Reynolds number.

The expression of the thrust efficiency can be presented as

$$\eta_{exp} = \frac{T_{exp} \cdot U_{exp}}{\overline{P}_{exp}}. \tag{4-21}$$

Based on the measured thrust force $T_{\exp}$, speed $U_{\exp}$, power consumption $\overline{P}_{exp}$, the experimental data of thrust efficiency $\eta_{\exp}$ was obtained. Figure 19e-h shows the experimental results of the thrust efficiency $\eta_{\exp}$. Based on Fig. 19e and f, it was found that inceptively, the efficiency of robotic swimmer in water increases as the frequency increases. With the frequency being relatively high, the efficiency decreases. Its thrust efficiency reaches the maximum when the frequency is approximately 1 *Hz*. It was also noticed that the IPMC swimmer has relatively high thrust efficiency at high input voltage. As the viscosity increases, the optimal frequency for the thrust efficiency increases, shown in Fig. 19g and h. The thrust efficiency of IPMC swimmer varies with different tails, and each has its optimal frequency. Generally, the thrust efficiency of tail 2 is higher than that of tail 1. Thus it was demonstrated that by increasing the input voltage as well as the size of IPMC, the thrust efficiency of the robotic swimmer can be improved. It

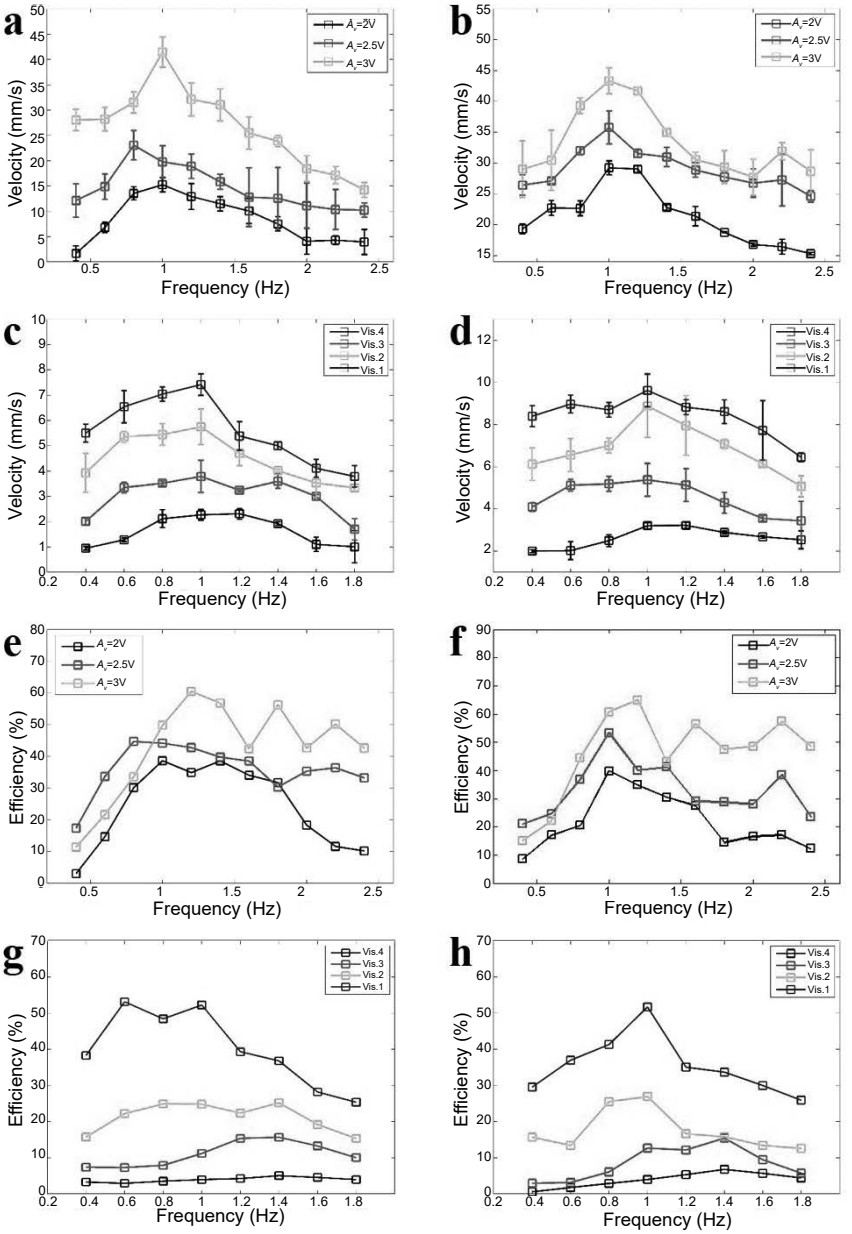

Figure 19. Experimental results of velocity and thrust efficiency. **(a)** Tail 1 in water (the viscosity is 1×10^{-6} m^2/s). **(b)** Tail 2 in water (the viscosity is 1×10^{-6} m^2/s). **(c)** Tail 1 in viscous fluid (A_v = 2.5 V). **(d)** Tail 2 in viscous fluid (A_v = 2.5 V). **(e)** Tail 1 in water (the viscosity is 1×10^{-6} m^2/s). **(f)** Tail 2 in water (the viscosity is 1×10^{-6} m^2/s). **(g)** Tail 1 in viscous fluid (A_v = 2.5 V). **(h)** Tail 2 in viscous fluid (A_v = 2.5 V). Original figures.

was also found that with the viscosity increasing, the Reynolds number and the thrust efficiency of the robotic swimmer decreases. One could indicate that the thrust efficiency of the robotic swimmer descends when its scale is reduced.

4.3 Brief Summary

In this section, two noteworthy efforts on the IPMC were proposed. Firstly, a physical based model of IPMC was presented. The model is based on the charge dynamics model of the polymer membrane and a microstructure model of the electrode. Secondly, an experimental approach was presented to test a robotic swimmer actuated by IPMC. The self-propelled speed, thrust force and power were measured and the thrust efficiency was calculated. With its characteristics of inherent softness, resilience and biocompatibility, IPMC has gained considerable research attention in the area of advanced materials, especially in actuation and sensing applications, such as artificial muscles, underwater actuators and advanced medical devices. The micro-fabrication of IPMCs is also enable scientists and engineers develop soft micro underwater actuators and sensors based on IPMC.

5. Conclusion

A general review of the material modeling, structural design, fabrication and experimental characterization of three representative advanced materials: SMA actuator, eGaIn elastomeric sensor and Ionic Polymer Metal Composites are provided in this chapter. The design principle of the SMA actuator in soft robots will tend to show more complex morphological changes to simulate the muscle movement of soft animals by advanced fabrication. In addition the SMA might be used more frequently as a sensor in the bio-structure as well. Besides application on soft robotics, strtechable elastimeric sensors also have important potential to be worn on the human body for motion tracking (Menguc et al. 2014, Vogt and Wood 2014), which offers outstanding performance in terms of compliancy and electrical properties. We also showed characteristics of inherent softness, resilience and biocompatibility of IPMC. We consider new types of actuators, sensors and new approaches of combing different methods for integrating simple-to-control, robust, low cost soft robotics are quite promising and have not yet been explored.

Acknowledgements

The authors thank Prof. Robert Wood and Nick Bartlett for their help on improving the manuscript. Also thanks for supporting from the National Science Foundation support projects, China under contract number 61403012 (to Li Wen), Beijing Science Foundation support projects under contract number 4154077 (to Li Wen) and National Science Foundation support projects, China under contract number 61333016 (to Tan Min).

References

Abdelnour, K., E. Mancia, S.D. Peterson and M. Porfiri. 2009. Hydrodynamics of underwater propulsors based on ionic polymer-metal composites: a numerical study. Smart Mater. Struct. 18(8).

Aureli, M., V. Kopman and M. Porfiri. 2010. Free-locomotion of underwater vehicles actuated by ionic polymer metal composites. Ieee-Asme T Mech. 15(4): 603–614.

Calisti, M., A. Arienti, F. Renda, G. Levy, B. Hochner, B. Mazzolai, P. Dario and C. Laschi. 2012. Design and development of a soft robot with crawling and grasping capabilities. 2012 Ieee International Conference on Robotics and Automation (Icra) 4950–4955.

Chen, Z., S. Shatara and X.B. Tan. 2010. Modeling of biomimetic robotic fish propelled by an ionic polymer-metal composite caudal fin. Ieee-Asme T Mech. 15(3): 448–459.

Chen, Z. and X.B. Tan. 2008. A control-oriented and physics-based model for ionic polymer-metal composite actuators. Ieee-Asme T Mech. 13(5): 519–529.

Cheung, Y.-N., Y. Zhu, C.-H. Cheng, C. Chao and W.W.F. Leung. 2008. A novel fluidic strain sensor for large strain measurement. Sensors and Actuators A: Physical 147(2): 401–408.

Chiechi, R.C., E.A. Weiss, M.D. Dickey and G.M. Whitesides. 2008. Eutectic gallium-indium (EGaIn): A moldable liquid metal for electrical characterization of self-assembled monolayers. Angew Chem. Int. Edit. 47(1): 142–144.

Cho, K.J., J.S. Koh, S. Kim, W.S. Chu, Y. Hong and S.H. Ahn. 2009. Review of manufacturing processes for soft biomimetic robots. Int. J. Precis Eng. Man. 10(3): 171–181.

Duerig, T. and A. Pelton. 1994. Ti-Ni shape memory alloys. Materials Properties Handbook: Titanium Alloys 1035–1048.

Fassler, A. and C. Majidi. 2013. Soft-matter capacitors and inductors for hyperelastic strain sensing and stretchable electronics. Smart Materials and Structures 22(5).

Fremond, M. 1996. Shape memory alloy. Springer.

Frutiger, A., J.T. Muth, D.M. Vogt, Y. Mengüç, A. Campo, A.D. Valentine, C.J. Walsh and J.A. Lewis. 2015. Capacitive soft strain sensors via multicore–shell fiber printing. Advanced Materials 1521–4095.

Hadi, A., A. Yousefi-Koma, M.M. Moghaddam, M. Elahinia and A. Ghazavi. 2010. Developing a novel SMA-actuated robotic module. Sensor Actuat a-Phys 162(1): 72–81.

Huang, W. 2002. On the selection of shape memory alloys for actuators. Mater. Design 23(1): 11–19.

Ilievski, F., A.D. Mazzeo, R.F. Shepherd, X. Chen and G.M. Whitesides. 2011. Soft robotics for chemists. Angewandte Chemie 123(8): 1930–1935.

Jala, V.R. and H. Ashrafiuon. 2006. Robust control of a class of mechanical systems actuated by shape memory alloys. P. Amer. Contr. Conf. 1(12): 5923–5928.

Jayender, J., R.V. Patel, S. Nikumb and M. Ostojic. 2008. Modeling and control of shape memory alloy actuators. Ieee T Contr. Syst. T 16(2): 279–287.

Joshipura, I.D., H.R. Ayers, C. Majidi and M.D. Dickey. 2015. Methods to pattern liquid metals. Journal of Materials Chemistry C 3(16): 3834–3841.

Kadowaki, A., T. Yoshikai, M. Hayashi and M. Inaba. 2009. Development of Soft Sensor Exterior Embedded with Multi-axis Deformable Tactile Sensor System. Ro-Man 2009: The 18th Ieee International Symposium on Robot and Human Interactive Communication, Vols. 1 and 2: 1164–1169.

Kate, M., G. Bettencourt, J. Marquis, A. Gerratt, P. Fallon, B. Kierstead, R. White and B. Trimmer. 2008. SoftBot: A soft-material flexible robot based on caterpillar biomechanics. Tufts University, Medford, MA, 2155.

Kier, W.M. and M.P. Stella. 2007. The arrangement and function of octopus arm musculature and connective tissue. J. Morphol. 268(10): 831–843.

Kim, D.H. 2011. Epidermal electronics (vol. 333, pg. 838, 2011). Science 333(6050): 1703–1703.

Kim, S., C. Laschi and B. Trimmer. 2013. Soft robotics: a bioinspired evolution in robotics. Trends in Biotechnology 31(5): 287–294.

Kim, S.J., S.M. Kim, K.J. Kim and Y.H. Kim. 2007. An electrode model for ionic polymer-metal composites. Smart Mater. Struct. 16(6): 2286–2295.

Lan, C.C. and Y.N. Yang. 2009. A computational design method for a shape memory alloy wire actuated compliant finger. J. Mech. Design 131(2).

Lee, S., H.C. Park and K.J. Kim. 2005. Equivalent modeling for ionic polymer-metal composite actuators based on beam theories. Smart Mater. Struct. 14(6): 1363–1368.

Leester-Schadel, M., B. Hoxhold, S. Demming and S. Buttgenbach. 2007. SMA micro actuators for active shape control, handling technologies, and medical applications. Microtechnologies for the New Millennium. 2007: 65891D-65891D-10.

Leester-Schadel, M., B. Hoxhold, C. Lesche, S. Demming and S. Buttgenbach. 2008. Micro actuators on the basis of thin SMA foils. Microsyst. Technol. 14(4-5): 697–704.

Lipomi, D.J., M. Vosgueritchian, B.C.K. Tee, S.L. Hellstrom, J.A. Lee, C.H. Fox and Z.N. Bao. 2011. Skin-like pressure and strain sensors based on transparent elastic films of carbon nanotubes. Nat. Nanotechnol. 6(12): 788–792.

Majidi, C., R. Kramer and R.J. Wood. 2011. A non-differential elastomer curvature sensor for softer-than-skin electronics. Smart Materials and Structures 20(10).

Mao, S.X., E.B. Dong, H. Jin, M. Xu, S.W. Zhang, J. Yang and K.H. Low. 2014. Gait study and pattern generation of a starfish-like soft robot with flexible rays actuated by SMAs. J. Bionic. Eng. 11(3): 400–411.

Margheri, L., C. Laschi and B. Mazzolai. 2012. Soft robotic arm inspired by the octopus: I. From biological functions to artificial requirements. Bioinspir. Biomim. 7(2).

Mazzolai, B., L. Margheri, M. Cianchetti, P. Dario and C. Laschi. 2012. Soft-robotic arm inspired by the octopus: II. From artificial requirements to innovative technological solutions. Bioinspir. Biomim. 7(2).

Mbemmo, E., Z. Chen, S. Shatara and X.B. Tan. 2008. Modeling of biomimetic robotic fish propelled by an ionic polymer-metal composite actuator. 2008 Ieee International Conference on Robotics and Automation, Vols. 1-9, 1050-4729689-694.

Menciassi, A., S. Gorini, G. Pemorio and P. Dario. 2004. A SMA actuated artificial earthworm. 2004 Ieee International Conference on Robotics and Automation, Vols. 1–5, Proceedings, 1050-47293282-3287.

Menguc, Y., Y.L. Park, H. Pei, D. Vogt, P.M. Aubin, E. Winchell, L. Fluke, L. Stirling, R.J. Wood and C.J. Walsh. 2014. Wearable soft sensing suit for human gait measurement. Int. J. Robot Res. 33(14): 1748–1764.

Muth, J.T., D.M. Vogt, R.L. Truby, Y. Menguc, D.B. Kolesky, R.J. Wood and J.A. Lewis. 2014. Embedded 3D printing of strain sensors within highly stretchable elastomers. Advanced Materials 26(36): 6307–6312.

Nemat-Nasser, S. and J.Y. Li. 2000. Electromechanical response of ionic polymer-metal composites. J. Appl. Phys. 87(7): 3321–3331.

Park, J., I. You, S. Shin and U. Jeong. 2015. Material approaches to stretchable strain sensors. ChemPhysChem. 1439–7641.

Park, Y.L., B.R. Chen and R.J. Wood. 2012. Design and fabrication of soft artificial skin using embedded microchannels and liquid conductors. Ieee Sens. J. 12(8): 2711–2718.

Peterson, S.D., M. Porfiri and A. Rovardi. 2009. A particle image velocimetry study of vibrating ionic polymer metal composites in aqueous environments. Ieee-Asme T Mech. 14(4): 474–483.
Porfiri, M. 2009. Influence of electrode surface roughness and steric effects on the nonlinear electromechanical behavior of ionic polymer metal composites. Phys. Rev. E. 79(4).
Prempraneerach, P., F. Hover and M. Triantafyllou. 2003. The effect of chordwise flexibility on the thrust and efficiency of a flapping foil. In Proc. 13th Int. Symp. on Unmanned Untethered Submersible Technology: special session on bioengineering research related to autonomous underwater vehicles, New Hampshire.
Quillin, K.J. 1999. Kinematic scaling of locomotion by hydrostatic animals: ontogeny of peristaltic crawling by the earthworm lumbricus terrestris. Journal of Experimental Biology 202(6): 661–674.
Romano, R. and E.A. Tannuri. 2009. Modeling, control and experimental validation of a novel actuator based on shape memory alloys. Mechatronics 19(7): 1169–1177.
Shahinpoor, M. and K.J. Kim. 2000. The effect of surface-electrode resistance on the performance of ionic polymer-metal composite (IPMIC) artificial muscles. Smart Mater. Struct. 9(4): 543–551.
Shahinpoor, M. and K.J. Kim. 2001. Ionic polymer-metal composites: I. Fundamentals. Smart Mater. Struct. 10(4): 819–833.
Shahinpoor, M. and K.J. Kim. 2005. Ionic polymer-metal composites: IV. Industrial and medical applications. Smart Mater. Struct. 14(1): 197–214.
Shen, Q., K.J. Kim and T.M. Wang. 2014. Electrode of ionic polymer-metal composite sensors: Modeling and experimental investigation. J. Appl. Phys. 115(19).
Shen, Q., T.M. Wang, J.H. Liang and L. Wen. 2013. Hydrodynamic performance of a biomimetic robotic swimmer actuated by ionic polymer-metal composite. Smart Materials and Structures 22(7).
Shepherd, R.F., F. Ilievski, W. Choi, S.A. Morin, A.A. Stokes, A.D. Mazzeo, X. Chen, M. Wang and G.M. Whitesides. 2011. Multigait soft robot. Proceedings of the National Academy of Sciences 108(51): 20400–20403.
Smooth-on. Ecoflex (R) Series / Super-Soft, Addition Cure Silicone Rubbers. In Smooth-on Inc.
Sreekumar, M., T. Nagarajan, M. Singaperumal, M. Zoppi and R. Molfino. 2007. Critical review of current trends in shape memory alloy actuators for intelligent robots. Ind. Robot 34(4): 285–294.
Sun, J.Y., C. Keplinger, G.M. Whitesides and Z.G. Suo. 2014. Ionic skin. Advanced Materials 26(45): 7608–7614.
Teh, Y.H. and R. Featherstone. 2008. An architecture for fast and accurate control of shape memory alloy actuators. Int. J. Robot Res. 27(5): 595–611.
Trimmer, B. and J. Issberner. 2007. Kinematics of soft-bodied, legged locomotion in Manduca sexta larvae. Biol. Bull-Us 212(2): 130–142.
Trueman, E.R. 1975. Locomotion of soft-bodied animals. Edward Arnold.
Vogt, D.M., Y.L. Park and R.J. Wood. 2013. Design and characterization of a soft multi-axis force sensor using embedded microfluidic channels. Ieee Sens. J. 13(10): 4056–4064.
Vogt, D.M. and R.J. Wood. 2014. Wrist angle measurements using soft sensors. In IEEE Sensors Conf.
Wang, T.M., Q. Shen, L. Wen and J.H. Liang. 2012a. On the thrust performance of an ionic polymer-metal composite actuated robotic fish: Modeling and experimental investigation. Sci. China Technol. Sc. 55(12): 3359–3369.
Wang, T.M., Z.Y. Shi, D. Liu, C. Ma and Z.H. Zhang. 2012b. An accurately controlled antagonistic shape memory alloy actuator with self-sensing. Sensors-Basel 12(6): 7682–7700.
Yamada, T., Y. Hayamizu, Y. Yamamoto, Y. Yomogida, A. Izadi-Najafabadi, D.N. Futaba and K. Hata. 2011. A stretchable carbon nanotube strain sensor for human-motion detection. Nat. Nanotechnol. 6(5): 296–301.

Yim, W., J. Lee and K.J. Kim. 2007. An artificial muscle actuator for biomimetic underwater propulsors. Bioinspir. Biomim. 2(2): S31–S41.
Zheng, T.J., Y.W. Yang, D.T. Branson, R.J. Kang, E. Guglielmino, M. Cianchetti, D.G. Caldwell and G.L. Yang. 2014. Control design of shape memory alloy based multi-arm continuum robot inspired by octopus. C Ind. Elect. Appl. 2156-23181108-1113.